

This is an Open Access document downloaded from ORCA, Cardiff University's institutional repository: <https://orca.cardiff.ac.uk/id/eprint/95429/>

This is the author's version of a work that was submitted to / accepted for publication.

Citation for final published version:

Brenny, Benjamin J. M., Beggs, Daryl M. , van der Wel, Ruben E. C., Kuipers, L. and Polman, Albert 2016. Near-infrared spectroscopic cathodoluminescence imaging polarimetry on silicon photonic crystal waveguides. *ACS Photonics* 3 (11) , pp. 2112-2121. 10.1021/acsphotonics.6b00557

Publishers page: <http://dx.doi.org/10.1021/acsphotonics.6b00557>

Please note:

Changes made as a result of publishing processes such as copy-editing, formatting and page numbers may not be reflected in this version. For the definitive version of this publication, please refer to the published source. You are advised to consult the publisher's version if you wish to cite this paper.

This version is being made available in accordance with publisher policies. See <http://orca.cf.ac.uk/policies.html> for usage policies. Copyright and moral rights for publications made available in ORCA are retained by the copyright holders.



# Near-infrared spectroscopic cathodoluminescence imaging polarimetry on silicon photonic crystal waveguides

Benjamin J. M. Brenny,<sup>†</sup> Daryl M. Beggs,<sup>‡,¶</sup> Ruben E. C. van der Wel,<sup>†</sup> L.  
(Kobus) Kuipers,<sup>†</sup> and Albert Polman<sup>\*,†</sup>

<sup>†</sup>*Center for Nanophotonics, FOM Institute AMOLF, Science Park 104,  
1098 XG Amsterdam, The Netherlands*

<sup>‡</sup>*Centre for Quantum Photonics, H.H. Wills Physics Laboratory, University of Bristol,  
Tyndall Avenue, Bristol BS8 1TL, United Kingdom*

<sup>¶</sup>*School of Physics and Astronomy, Cardiff University, Cardiff CF24 3AA, United Kingdom*

E-mail: polman@amolf.nl

## Abstract

1  
2 We measure polarization- and wavelength-resolved spectra and spatial emission  
3 intensity distributions from silicon photonic crystal waveguides in the near-infrared  
4 spectral range using spectroscopic cathodoluminescence imaging polarimetry. A 30  
5 keV electron beam, incident along the surface normal of the sample, acts as an ultra-  
6 broadband and deeply subwavelength excitation source. For photonic crystal wave-  
7 guides with a broad range of design parameters, we observe a dominant emission inten-  
8 sity distribution that is strongly confined to the waveguide. For a period of 420 nm  
9 and a hole radius of 120 nm, this occurs at a wavelength of 1425 nm. The polarization-  
10 resolved measurements demonstrate that this feature is fully linearly polarized along

11 the waveguide axis. Comparing the modal pattern and polarization to calculations  
12 of the electric field profiles confirms that we measure the odd TE waveguide mode  
13 of the system. This result demonstrates that the electron beam can couple to modes  
14 dominated by in-plane field components in addition to the more commonly observed  
15 modes dominated by out-of-plane field components. From the emission directionality,  
16 we conclude that we sample a leaky portion of the odd waveguide mode.

## 17 **Keywords**

18 Cathodoluminescence, photonic crystal waveguide, polarimetry, near-infrared

19 Photonic crystals, materials with a periodically varying dielectric function, can manip-  
20 ulate the propagation of light in a controlled way. They create a photonic band gap that  
21 prevents light from propagating in certain directions for certain frequencies.<sup>1-5</sup> The photonic  
22 band gap can lead to a strong confinement of light, and engineered defects allow the creation  
23 of photonic crystal cavities and waveguides. Photonic crystal cavities can have long photon  
24 lifetimes and small mode-volumes,<sup>6-8</sup> leading to strong light-matter interactions and enabling  
25 applications such as low threshold lasers.<sup>9-12</sup> Photonic crystal waveguides are strongly dis-  
26 persive, and can slow light down, which also leads to enhanced light-matter interactions.<sup>13-21</sup>  
27 This strong dispersion allows such waveguides to serve as many components and building  
28 blocks in photonic integrated circuits, such as splitters, switches or multiplexers.<sup>18,22-25</sup> To  
29 fully exploit the many applications of photonic crystal waveguides, it is essential to measure  
30 the propagation and confinement of light at a subwavelength scale. This cannot be achieved  
31 by conventional microscopy techniques. Near-field scanning optical microscopy (NSOM),  
32 which uses subwavelength probes or apertures to detect or scatter the near field of these  
33 structures,<sup>26-30</sup> has enabled measurements of the field components of the optical near field  
34 just above the waveguide.<sup>31,32</sup>

35 Cathodoluminescence (CL) spectroscopy is an alternative technique that can be used

36 to study nanophotonic structures, coupling to and probing the field distributions inside.  
37 A high-energy electron beam is used as a nanoscale optical excitation source in which the  
38 time-varying electromagnetic field of the electron couples to the local optical modes of the  
39 system as it traverses the sample.<sup>33-35</sup> This mechanism, which is fully described by Maxwell's  
40 equations, is fundamentally similar to that of the oscillating electric field of a laser beam  
41 coupling to optical excitations. In CL, the light scattered from these optical modes to the  
42 far field is detected. The short interaction time of the electron with the structure (a few  
43 fs) results in a broadband excitation spectrum (typically several  $\mu\text{m}$ , down into the deep  
44 UV). The high excitation resolution of CL is only limited by the extent of the electric field  
45 about the electron trajectory and the spread of the beam in the sample. This allows one to  
46 explore the radiative local density of states (LDOS) at deeply subwavelength scales.<sup>34,36</sup> The  
47 electron forms a noninvasive probe of the optical properties inside the material. Recently,  
48 it has become possible to measure the full polarization distribution of CL emission as a  
49 function of angle by using polarimetry.<sup>37</sup> These properties have made CL a powerful, deeply  
50 subwavelength characterization technique,<sup>38-44</sup> allowing measurements of the confinement  
51 and dispersion of plasmonic and dielectric photonic crystal cavities in the visible spectral  
52 range.<sup>34,45-47</sup>

53 In this article, we apply spectroscopic cathodoluminescence imaging polarimetry in the  
54 near-infrared (NIR) spectral range to study the confinement and polarization of propagating  
55 photonic crystal waveguide modes. More specifically, we examine how the electron beam  
56 couples to the electromagnetic eigenmodes of the system. CL emission is typically dom-  
57 inated by modes with primarily out-of-plane electric field components (hereafter referred  
58 to as out-of-plane or TM modes). Modes with primarily in-plane electric field components  
59 (hereafter referred to as in-plane or TE modes) are usually not significant. These structures,  
60 however, possess different band structures for TE and TM polarization and support two well  
61 defined modes for TE polarization, denoted as even and odd.<sup>5,48,49</sup> We demonstrate that  
62 CL imaging polarimetry enables direct identification and spatial mapping of the modal field

63 distribution in the photonic crystal waveguides. The CL emission is dominated by the odd  
64 TE waveguide mode, with measurements showing good agreement with calculations of the  
65 modal field intensities. Using photonic crystal waveguides as a well-known model system,  
66 we demonstrate the direct excitation of in-plane TE modes by the electron beam. We show  
67 that the excitation process involves a complex combination of coupling of the electron beam  
68 to multiple field components of the propagating TE modes.

## 69 **Experiment**

70 Silicon photonic crystal waveguides (PCWGs) were fabricated on silicon-on-insulator (SOI)  
71 wafers with a 220 nm thick silicon layer on top of a 1  $\mu\text{m}$  silica layer on a silicon substrate.  
72 Electron beam lithography was used to pattern the waveguides, followed by reactive ion  
73 etching to etch through the top silicon layer. A wet HF etch was used to remove part of the  
74 silica layer and obtain a suspended PCWG. Reference measurements in the visible and NIR  
75 spectral ranges demonstrate that a residual silica layer remains, since we observe character-  
76 istic silica defect-related emission peaks. Two different samples were studied; here we only  
77 discuss sample 1, showing data for sample 2 in Figure S1 of the Supporting Information.  
78 Figure 1(a) shows a SEM image of one of the PCWGs on sample 1 examined here, with a  
79 length of 90  $\mu\text{m}$  and a total width of the photonic crystal section of 10  $\mu\text{m}$ . The PCWG is  
80 composed of a hexagonal array of holes with one missing row of holes (W1 waveguide).<sup>5,49,50</sup>  
81 Five waveguides were made on sample 1 with the same period  $a=420$  nm and hole radii  
82 varying in the range  $\sim 105$ – $125$  nm. Figure 1(b) shows a close-up of the waveguide section  
83 for the most studied structure (denoted as WG2), which has a period  $a=420$  nm and a hole  
84 radius  $r=120$  nm.

85 The TE band structure of WG2 is shown in Figure 1(c), calculated using an open-source  
86 MIT Photonic Bands (MPB) frequency domain mode-solver.<sup>51</sup> TE polarization corresponds  
87 to electric fields that are primarily oriented in the plane of the waveguide slab (fully so only

88 in the vertical plane of symmetry  $z=0$ ). The gray bands represent modes that make up a  
89 continuum below and above the photonic band gap, which opens up between normalized  
90 frequencies of  $\sim 0.25$ – $0.32$ , corresponding to free space wavelengths of  $\sim \lambda_0=1300$ – $1700$  nm.  
91 The discrete bands at the lower right are index-guided bands,<sup>5</sup> confined by total internal  
92 reflection in the slab. The band structure is very sensitive to the period, hole size and slab  
93 thickness.<sup>52</sup>

94 Removing rows of holes leads to allowed modes within this band gap,<sup>48–50,53</sup> that are  
95 confined vertically by index-guiding (total internal reflection), but horizontally by the band  
96 gap of the photonic crystal. For a single row of missing holes there are two TE waveguide  
97 modes in the band gap: an even mode with a symmetric field distribution and an odd mode  
98 with an anti-symmetric distribution for the in-plane transverse electric field component.<sup>13,48</sup>  
99 The even mode has been studied intensely due to its anomalous dispersion and vanishing  
100 group velocity over a large range of wavevectors when approaching the edge of the Brillouin  
101 zone.<sup>13,14,18,19</sup> The odd mode is less well studied, but also displays slow light over a broad  
102 range of wavevectors (see Figure 1(c)). The dashed line in the figure represents the light line  
103 in air; modes to the left will be leaky and modes to the right are guided in the waveguide  
104 slab.

105 In addition to TE modes, the photonic crystal possesses TM modes, with an electric field  
106 perpendicular to the waveguide slab at  $z=0$ . Such modes are usually excited efficiently by  
107 CL,<sup>33</sup> since the moving electron acts as a vertically polarized source. In Figure S4 of the  
108 Supporting Information we show the band structure for TM polarization. We find that there  
109 is a small photonic band gap for wavelengths in the range  $\sim \lambda_0=1100$ – $1200$  nm with two  
110 waveguide modes within. In the spectral range of the TE band gap, the TM band structure  
111 exhibits a continuum of modes. Modes inside or near the band gap are usually localized to  
112 the waveguide, while modes in the continuous bands are more delocalized over the photonic  
113 crystal.<sup>5,48</sup> The PCWGs studied here are specifically designed for high quality TE modes  
114 rather than TM modes, so the former will typically exhibit a higher LDOS. There are thus

115 multiple possible sources of emission, for both TE and TM polarization, when exciting these  
116 Si PCWGs with swift electrons.

117 Figures 1(d,e) shows calculations of the electric field intensity distributions for the odd  
118 (d) and even (e) TE polarized modes at  $\lambda_0=1450$  nm, using the MPB code. We calculate  
119 the  $E_x$ ,  $E_y$  and  $E_z$  field components as a function of position and wavevector within a  
120 small frequency range, then integrate over all  $k$  and field components. For simplicity, these  
121 calculations are all 2D, performed at  $z=0$  so  $E_z$  is strictly 0 as well, but this does not affect  
122 the relevant features of these in-plane modes (see Figure S5 of the Supporting Information  
123 for 3D calculations of  $E_z$ ). All 2D calculations are normalized to the same overall maximum  
124 (obtained for TE at  $\lambda_0=1500$  nm, not shown here) and the holes are masked (the intensity  
125 inside the holes is set to zero) to better compare the results to the measurements. For more  
126 details about the calculation procedure, see the Methods Section. We observe that both  
127 odd (Figure 1(d)) and even (Figure 1(e)) modes display sharp high intensity features along  
128 the center of the waveguide. The odd mode, however, exhibits a more localized, distinct  
129 and bright modal distribution pattern. These two modes are differentiated by the symmetry  
130 of the in-plane field component transverse to the waveguide propagation direction, which  
131 becomes clear when examining the real or imaginary amplitudes (not shown here) but not  
132 apparent for the field intensity presented here. The modes are, however, also dominated by  
133 different field components (see Figure S7 of the Supporting Information).

134 Calculations for TM polarization in the range  $\lambda_0=1430$ – $1500$  nm are shown in Figure S4  
135 of the Supporting Information, but exhibit no sharp features such as the ones on display for  
136 TE polarization.

137 Figure 1(f) depicts a schematic representation of the CL setup.<sup>34,37,54</sup> The 30 keV electron  
138 beam excites the sample and a parabolic mirror collects the subsequent emission and directs  
139 it onto a fiber connected to a NIR spectrometer. The small size of the electron probe and  
140 precise scanning capabilities of the SEM allow us to perform spectrally- and spatially-resolved  
141 scans of the PCWGs. We also measure the spectrally-resolved polarization of the emission

142 by adding a movable, vertical slit to the optical path. In general, the polarization of the  
143 emitted radiation can change as it reflects off the mirror, due to its curved shape. The slit  
144 selects the central part of the mirror and conserves the emission polarization,<sup>55,56</sup> integrating  
145 over zenithal angles for a narrow range of azimuthal angles. We perform measurements for  
146 different positions of the slit and orientations of the waveguide with respect to the mirror to  
147 determine the polarization state and emission directionality (see Supporting Information).  
148 We combine a quarter-wave plate (QWP) and linear polarizer (Pol.) to determine the Stokes  
149 parameters, which fully describe the polarization state of the emitted light.<sup>37,57</sup> This allows  
150 for the separation of polarized and unpolarized light, as well as the retrieval of different field  
151 components inside the structure and the relative phase difference between them.<sup>57</sup> Measuring  
152 the emission polarization thus allows the mapping of the electric field components. The  
153 Methods Section describes the experimental setup and measurement protocol in more detail.  
154 For the measurements described in the main text, all waveguides are oriented along the  
155 y-axis, as defined by the coordinate system in Figure 1(f).

## 156 **Near-infrared spatially-resolved cathodoluminescence**

157 Figure 2 presents 2D spatial CL intensity maps from WG2, at wavelengths of  $\lambda_0=1170$  nm (a),  
158  $\lambda_0=1185$  nm (b),  $\lambda_0=1400$  nm (c), and  $\lambda_0=1425$  nm (d), all averaged over a 20 nm bandwidth.  
159 Combining the raw data with the spectral response of the system and in-situ beam current  
160 measurements allow us to determine the CL emission probability (number of photons emitted  
161 per incoming electron, per unit bandwidth of  $\text{nm}^{-1}$ ).<sup>58</sup> We additionally correct the data for  
162 the dark response of the detector as well as for signal from the remaining silica and the silicon  
163 substrate, which contributes a broadband response and a peak at  $\lambda_0=1275$  nm. To do so, we  
164 use a reference spectrum measured in one of the holes, which has no contribution from the  
165 waveguide or photonic crystal modes. In the Supporting Information, we show additional  
166 measurements for a sample with a different period (Figure S1), for the input section of WG2

167 (Figure S2) and for WG2 closer to the visible spectral range (Figure S3).

168 The measurements at  $\lambda_0=1170$  nm and  $\lambda_0=1185$  nm (Figures 2(a,b)), exhibit an overall  
169 similarity, with high intensity at the inner edges of the holes lining the waveguide and darker  
170 spots along the waveguide at positions in between four holes. These two positions are denoted  
171 as A and B in Figures 2(a,c). Figure 2(b) exhibits a distinct enhanced intensity at the edges  
172 of the holes outside of the waveguide, compared to Figure 2(a). Figures 2(c,d) show data  
173 at  $\lambda_0=1400$  nm and  $\lambda_0=1425$  nm, displaying a high intensity at the inner edges of the holes  
174 lining the waveguide, which wrap around the hole edges more than for the data at shorter  
175 wavelengths. The center of the waveguide exhibits high intensity features at positions that  
176 were dark for  $\lambda_0=1170$  nm and  $\lambda_0=1185$  nm. At  $\lambda_0=1425$  nm these peaks are most intense,  
177 while the region around the waveguide has a lower relative intensity than for  $\lambda_0=1400$  nm.  
178 The fact that the signal for  $\lambda_0=1425$  nm is very strongly confined to the waveguide suggests  
179 it is related to a waveguide mode.

180 The features at  $\lambda_0=1170$  nm and  $\lambda_0=1185$  nm occur in the upper band of the TE band  
181 structure (see Figure 1(c)), that represent modes that are delocalized over the waveguide  
182 and surrounding holes,<sup>5,48</sup> as seen in Figures 2(a,b). In addition to TE modes, TM modes  
183 could also be responsible for this measured emission. As Figure S4 of the Supporting In-  
184 formation demonstrates, there is a small TM photonic band gap for wavelengths in the  
185 range  $\sim \lambda_0=1100$ – $1200$  nm with two waveguide modes within. The emission patterns at  
186  $\lambda_0=1400$  nm and  $\lambda_0=1425$  nm occur in the middle of the TE photonic band gap, where the  
187 even and odd waveguide modes are present. For TM polarization these wavelengths are in  
188 the continuum of modes below the TM band gap, where one expects modes that are more  
189 delocalized from the waveguide, unlike the patterns observed here that are strongly confined  
190 to the waveguide. Comparing the measurements to the calculations of the modal field distri-  
191 butions in Figures 1(d,e), excellent agreement is observed between the data and the odd TE  
192 waveguide mode, while calculations for TM polarization exhibit a very different and weaker  
193 response (Figure S4 of the Supporting Information). This indicates that the out-of-plane

194 electron beam is coupling most strongly to an in-plane mode, which seems counter-intuitive  
195 at first.

196 The electron beam principally couples to field components that are parallel to the electron  
197 trajectory.<sup>33</sup> For electrons propagating along  $z$ , this should lead to preferential coupling to  
198 the TM modes, yet we clearly observe patterns identical to TE modes. Our 2D calculations  
199 for TE polarization are performed at  $z=0$ , where  $E_z$  is strictly zero. The membrane does have  
200 a finite thickness, however, so  $E_z$  has nonzero components for other  $z$ -coordinates.<sup>5</sup> We can,  
201 for example, expect vertical components at the edges of the holes.<sup>32</sup> To verify this we have  
202 performed a set of 3D MPB calculations, determining the modal fields for different values of  
203  $z$ . We display the calculated  $E_z$  in Figure S5 of the Supporting information, showing that  
204 the hole edges indeed exhibit a distinct  $E_z$  component. Considering the high intensity in  
205 the middle of the waveguide, the even mode is symmetric with respect to the center, for  
206 the transverse in-plane field component (perpendicular to the waveguide axis), so there is no  
207 field gradient across the central axis and the electric field is expected to remain in-plane. The  
208 odd mode however is anti-symmetric for the transverse in-plane field component, exhibiting  
209 a field gradient across the central axis and a node at the very center where the field switches  
210 sign. This flip in the fields is accompanied by a nonzero  $E_z$  component in the center for  
211 different (nonzero)  $z$ -coordinates, explaining why we preferentially measure the odd mode.  
212 This is also confirmed by Figure S5, showing that the odd mode has nonzero values of  $E_z$   
213 along the waveguide center while  $E_z$  of the even mode is close to zero and the odd mode also  
214 has a higher intensity overall than the even mode. The  $E_z$  intensity locally reaches  $\sim 15\%$   
215 of the maximum value of the total intensity for the odd mode and  $\sim 5\%$  for the even mode.

216 Another source of coupling between the electrons and the TE modes is the fact that  
217 scattering of the incident electrons inside the silicon membrane leads to a spread in their  
218 propagation directions, allowing for direct coupling to in-plane field components.<sup>34</sup> The scat-  
219 tering increases for lower electron energies, which should result in stronger coupling to the  
220 in-plane components. We do indeed observe higher intensities from the modal peaks using

221 10 keV instead of 30 keV (not shown here).

222 Both the 3D distribution of the electric fields with locally significant  $E_z$  components  
223 aligned with the incident electrons and electron scattering inside the silicon slab allowing for  
224 alignment with the  $E_x$  and  $E_y$  components play a role in exciting the in-plane TE modes in  
225 the PCWG slab. Although TM modes should still have a better overlap with the electron  
226 beam, the band structure is dominated by a continuum of modes. For TE, however, there  
227 is a clear band gap with well defined waveguide modes that can stand out, as they have a  
228 higher local density of states than the delocalized TM modes.

## 229 **Spectroscopic polarimetry**

230 To further confirm the TE nature of the measured modes, we need to study the polarization-  
231 filtered spectral response of the waveguide. We begin by examining non-filtered spectra in  
232 Figure 3(a), which presents the CL spectra at the inner edge of the hole lining the waveguide  
233 (position A in Figure 2(a), in red) and in the center of the waveguide between four holes  
234 (position B in Figure 2(c), in blue). Both positions are dominated by a peak at  $\lambda_0 \sim 1425$  nm.  
235 The spectrum for position A also exhibits additional smaller peaks at  $\lambda_0 \sim 1225$  nm and  
236 1175 nm, for which the CL intensity distribution was plotted in Figures 2(a,b).

237 The modal structure of PCWGs is sensitive to small changes in the geometry, which is  
238 demonstrated in Figure 3(b), where we have measured the spectra for five different waveg-  
239 uides (WG1–WG5) with increasing hole sizes, all measured for excitation position A. We  
240 observe a clear redshift of the spectral features for decreasing hole size. We note a variability  
241 in the intensity as well as an increasing contribution of a second peak on the blue side of  
242 the main emission peak, for decreasing hole size. The inset of Figure 3(b) shows the main  
243 peak resonance wavelength as a function of the hole radius, as determined from SEM im-  
244 ages. A  $\sim 20$  nm change in hole radius leads to a  $\sim 80$  nm shift in the resonance wavelength,  
245 underlining the sensitivity of the modes to geometrical parameters.<sup>52</sup>

246 To measure the polarization-resolved spectra, we first place the vertical movable slit  
247 with a width of 3 mm in the optical path. We find that both peaks at  $\lambda_0 \sim 1175$  nm and  
248  $\lambda_0 \sim 1425$  nm in the spectra from Figure 3(a) exhibit maximum intensity in the middle of the  
249 mirror, for orthogonal orientations of the waveguide relative to the mirror, indicating that the  
250 emission direction is close to the surface normal. We can now use polarimetry to determine  
251 the polarization state of the emitted radiation, which allows the retrieval of the electric field  
252 orientations inside the structure. We assume the interface does not significantly alter the  
253 field orientations for emission close to the surface normal. For these measurements we do  
254 not separately subtract the signal from the substrate. More details on the implementation  
255 can be found in the Methods Section and the Supporting Information.

256 We display the Stokes parameters for excitation position A on WG2 oriented along the  $y$ -  
257 axis in Figure 3(c).  $S_0$  corresponds to the total intensity, where we have not corrected for the  
258 emission from the substrate.  $S_3$  determines the ellipticity and handedness of the polarization.  
259 We do not expect circularly polarized emission from the structure, but for linearly polarized  
260 emission the measured reflection off of the curved surface of the mirror can lead to a circular  
261 component. This is only negligible if the slit that spatially filters the emission is positioned  
262 at the center of the parabolic mirror, where the emitted and reflected rays lie in the same  
263 plane as the surface normal of the mirror. In that case the problem reduces to classical  
264 Fresnel reflection where the  $s$ - and  $p$ -polarizations (horizontal and vertical) are conserved.  
265 We find that  $S_3 \approx 0$  for all wavelengths, demonstrating that the slit is well aligned.  $S_2$ , which  
266 indicates the orientation of the principal axes of linearly polarized light, is also close to zero  
267 over all wavelengths. All of the polarized contribution is contained in  $S_1$ , meaning that  
268 the polarization is fully linear and either horizontal ( $S_1 > 0$ ) or vertical ( $S_1 < 0$ ). Horizontal  
269 polarization corresponds to emission polarized along the  $y$ -axis and vertical polarization  
270 corresponds to emission polarized along either the  $z$ -axis or the  $x$ -axis of the coordinate  
271 system (see Figure 1). We find that the dominant peak at  $\lambda_0 = 1425$  nm is polarized along the  
272 waveguide axis ( $y$ -axis for data shown here). A TM mode predominantly has an out-of-plane

273 electric field, i.e. along the z-axis and would therefore be measured as a vertical polarization  
274 for any orientation of the waveguide. In-plane TE modes, with electric field components  
275 typically along the waveguide axis or orthogonal to it, will be along either the x- or y-axes for  
276 carefully aligned orthogonal orientations of the waveguide. Their emission will be measured  
277 up as a horizontal polarization for one orientation and vertical for the other orthogonal  
278 orientation. Experiments using such orthogonal orientations of the waveguide (see Figure S6  
279 of the Supporting Information) result in orthogonal horizontal/vertical polarizations for all  
280 of the measured peaks. This demonstrates that all of the features are related to TE and  
281 not to TM modes, confirming once again that the electron beam can couple to in-plane  
282 excitations.

283 Using polarimetry allows us to separate the polarized (in red) and unpolarized (in gray)  
284 contributions to the spectra from Figure 3(c). Compared to the measured total intensity  
285 S0 we can clearly see that most of the signal, including the small peak at  $\lambda_0 \sim 1275$  nm, is  
286 unpolarized. We ascribe this unpolarized emission to the luminescence from the substrate.  
287 The peaks in the polarized contribution all correspond to modal features in Figure 2 (for  
288 both excitation positions A and B) and demonstrates the power of polarimetry to filter out  
289 these unpolarized contributions to obtain clear resonances with a high contrast.

290 Figures 4(a,b) show measurements of the polarization-filtered CL emission intensity dis-  
291 tributions from WG2, at  $\lambda_0=1425$  nm, for x and y polarization. Clearly, the emission is  
292 polarized along the waveguide axis y. Figures 4(c,d) show the calculated modal field inten-  
293 sity distributions (summed over  $k$ ) at  $\lambda_0=1450$  nm for the  $E_y$  (c) and  $E_x$  (d) components.  
294 We observe good qualitative agreement between the calculations and the measurements, es-  
295 pecially for the  $E_y$  component, while the calculated  $E_x$  intensity is more intense than the  
296 x-polarized data. At this wavelength the mode is guided, but it is close to the light line. The  
297 emission can still escape, due to scattering from roughness and imperfections for instance.  
298 The emission directionality towards the surface normal ( $k \sim 0$ ) suggests, however, that the  
299 mode can radiate out directly, indicating that the leaky part of the odd mode contributes to

300 the measured emission.

301 For this reason we also calculate the field profiles at  $\lambda_0=1500$  nm, where the dispersion  
302 relation of odd mode intersects the frequency window of the calculation for regions of  $k$  both  
303 above the light line (close to  $k=0$ ) and below the light line. The modal intensity distributions  
304 for  $k$  above the light line show very good agreement with the data, as we can observe in  
305 Figure 4(e) for the  $E_y$  intensity and in Figure 4(f) for the  $E_x$  intensity. The intensity profiles  
306 for  $k$  below the light line differ more from the measured emission profiles (see Figure S7 of  
307 the Supporting Information). Comparing the measurements to the calculations, we find that  
308 the intensity distributions and relative intensities (for both polarizations) show agreement  
309 for both calculations, but there is clearly a better match with the leaky distributions at  
310  $\lambda_0=1500$  nm. The discrepancy in wavelength between measurement and calculation can be  
311 attributed to variations between the measured and calculated geometrical parameters, which  
312 we have shown to strongly impact the positions of all resonances in the spectra. We note  
313 that the calculations are not designed to determine field profiles in the leaky region above  
314 the light line, since they do not take into account nonzero values of  $k_z$ , which necessarily  
315 exist for leaky modes that radiate out of the waveguide to free space. Calculations in other  
316 systems, however, that do fully take leaky contributions into account, have shown that the  
317 mode can retain its overall field profile, even if it does become more lossy.<sup>59,60</sup> In our case  
318 this is advantageous, as the mode is radiating out of the structure more freely, allowing us  
319 to measure it directly.

320 CL spectroscopy proves to be a useful technique to measure modes in nanophotonic struc-  
321 tures, comparable to NSOM for example. In the case of NSOM, the near field is mapped  
322 with a nanoprobe that is brought into the evanescent field of the light in the nanostructure.  
323 As a result, different field components of both the electric and magnetic fields can be dis-  
324 tinguished,<sup>31,32</sup> allowing in-depth studies of confined modes at the nanoscale, including their  
325 dispersion. However, the image formation is complex and the interpretation of the experi-  
326 mental results is non-trivial. The nanoprobe used to perform NSOM measurements can, in

327 certain cases, perturb the system, so care must be taken in the processing and interpretation  
328 of the data. Another way to image confined modes is grating-assisted Fourier space imaging,  
329 in which light from below the light-line is scattered to the far field by a secondary grating  
330 and collected by a Fourier lens.<sup>61,62</sup> This approach permits one to determine the dispersion  
331 relation, symmetry, and interaction of confined modes, but the secondary grating can also  
332 perturb the system similarly to the NSOM nanoprobe and adds additional complexity to  
333 the fabrication. CL on the other hand is a noninvasive far field technique (the electrons  
334 excite, but do not perturb, the electromagnetic modes), measuring light both from leaky  
335 modes above the light line and from confined modes that scatter out due to defects. Unlike  
336 NSOM it probes the fields inside the structure, instead of the evanescent near field. Or  
337 rather, it does not directly measure the electric field, but the emission can be related to the  
338 radiative LDOS<sup>36</sup> and the excitation resolution is truly nanoscale ( $\sim 10$  nm).

## 339 **Conclusions**

340 In conclusion, we have demonstrated that an electron beam can be used to excite the prop-  
341 agating TE modes of a Si photonic crystal waveguide, despite them being dominated by  
342 in-plane field components. We applied, for the first time, spectroscopic cathodoluminescence  
343 imaging polarimetry in the near-infrared spectral range to directly image the modal field dis-  
344 tribution and image the emission and polarization with nanoscale resolution. Accordingly,  
345 the most striking feature that we observe is the odd TE waveguide mode of the structure,  
346 which exhibits a highly localized emission intensity distribution. Using spectroscopic po-  
347 larimetry we demonstrate that the emission of this mode is fully linearly polarized along the  
348 direction of the waveguide. This is supported by calculations of the electric field intensities  
349 which show good qualitative agreement with both the measured intensity distributions and  
350 polarization. Surprisingly, the vertically oriented electron beam can couple to this in-plane  
351 mode, as a result of nonzero contributions from the out-of-plane field component at different

352 heights within the waveguide. A redistribution of the electron trajectories due to scattering  
353 also plays a role. The emission peak corresponding to the odd waveguide mode is directional  
354 towards the surface normal, indicating that we sample a leaky part of the waveguide mode  
355 that radiates out of the structure. Spectroscopic cathodoluminescence imaging polarimetry  
356 is a powerful, noninvasive tool to measure light confinement, polarization and propagation  
357 at the nanoscale in photonic crystal waveguides and other complex nanophotonic structures.

## 358 **Methods**

### 359 **Cathodoluminescence measurements**

360 The measurements were performed in a FEI XL-30 SFEG (10–30 keV electron beam,  $\sim 30$ –  
361 46 nA current) equipped with a home-built CL system.<sup>34,37,54</sup> An aluminium parabolic mirror  
362 collects the emitted light and directs it outside of the microscope to an optical setup. We  
363 can measure the spectrum in the  $\lambda_0=350$ –1000 nm spectral range with a liquid-nitrogen-  
364 cooled back-illuminated silicon CCD array (Princeton Instruments Spec-10 100B) and in  
365 the  $\lambda_0=900$ –1600 nm spectral range with a liquid-nitrogen-cooled InGaAs photodiode ar-  
366 ray (Princeton Instruments OMA V). Due to the readout noise of the individual pixels, we  
367 smooth the spectra with a moving filter over a 2 nm bandwidth. We correct for the sys-  
368 tem response of the setup by using transition radiation from single crystal aluminium as a  
369 reference.<sup>58</sup> A Faraday cup integrated in the sample holder measures the current of the elec-  
370 tron beam, which in combination with the system response allows us to determine the CL  
371 emission probability. A quarter-wave plate (QWP, Thorlabs AQWP10M-1600) and linear  
372 polarizer (Pol., Moxtek PUBB01A50M) are used together to measure the full polarization  
373 state of the emitted radiation.<sup>37</sup> To measure the polarization we place a 3 mm wide slit in the  
374 beam path followed by the QWP and Pol., which offers a good balance between signal inten-  
375 sity and polarization contrast.<sup>55,56</sup> Because we focus all of the light passing through the slit  
376 onto the spectrometer, the measured polarization is averaged over the zenithal angles that

377 are collected. A series of six measurements for different combinations of the QWP and Pol.  
378 (horizontal/90°, vertical/0°, 45°, 135°, right- and left-handed circular) determine the Stokes  
379 parameters, which fully describe the polarization state of the light. Measurement errors can  
380 occur due to drift of the electron beam across the sample, bleaching or contamination leading  
381 to a reduction in the measured intensity, as well as fluctuations in the current and optical  
382 alignment of the mirror. For all spectral measurements we collect a dark reference spectrum  
383 where we blank the electron beam, subtracting this from the data in the post-processing  
384 stage.

## 385 Calculations

386 To calculate the modal fields of the photonic crystal waveguide, we calculated the eigenfre-  
387 quencies and complex field amplitudes  $E(r)$  using the MIT Photonics Band (MPB) code,<sup>51</sup>  
388 which is a plane-wave method that uses periodic boundary conditions to calculate the eigen-  
389 frequencies and eigenmodes of our PCWGs. The band structure diagrams were calculated  
390 with the full 3D version. In order to conserve computational resources, we implemented a  
391 2D version of the calculation using an effective index approximation to determine the field  
392 profiles. The effective index of the slab was chosen to be that of a 220 nm thick slab of silicon  
393 with the refractive index appropriate for each frequency range considered (for example for  
394 wavelengths around  $\lambda_0=1450$  nm, we used 3.484). This procedure yields an effective index  
395 of 2.873 for TE modes and 1.831 for TM modes at  $\lambda_0=1450$  nm. We determine the eigen-  
396 values between 99 % and 101 % of the desired frequency. The  $E_x$ ,  $E_y$ , and  $E_z$  field profiles  
397 (or eigenmodes) are calculated on a rectangular grid of points separated by  $a/16$ , ensuring  
398 that the eigenfrequencies are converged to better than 0.1 %. The modes are normalized  
399 such that  $\int_{\text{unit cell}} \epsilon(r) * |E(r)|^2 dr = 1$ . The calculations are performed for wavevectors in  
400 the first irreducible Brillouin zone, after which we use symmetry arguments to add the fields  
401 for different wavevectors with the correct weighting factor, over the full first Brillouin zone.  
402 Essentially, we sum the field intensities over all wavevectors  $\mathbf{k}$  of the modes that occur within

403 the frequency range of the calculation, at each position  $\mathbf{r}$ :

$$\frac{1}{(2\pi)^3} \sum_{n=1}^N \int_k |E_{n\mathbf{k}}^{(i)}(\mathbf{r})|^2 \delta(\omega - \omega_{n\mathbf{k}}) d\mathbf{k}. \quad i = x, y, z.$$

404 For the leaky/guided mode results we only sum over the wavevectors above/below the  
405 light line. The total field intensity is then determined by summing over all three field  
406 components. All of the resulting field intensity distributions are normalized to the maximum  
407 total intensity value for all wavelengths and polarizations (TE at  $\lambda_0=1500$  nm). The intensity  
408 inside the holes is set to zero to better compare the results to the measurements, since there  
409 is no polarizable material in the empty holes the electron beam does not produce radiation  
410 even if there can be a high field intensity and/or LDOS in the holes.

## 411 **Supporting Information Available**

412 The Supporting Information contains measured data from an additional sample, an input  
413 section of the waveguide studied here and for shorter wavelengths. Additionally, 2D calcu-  
414 lations for TM polarization, 3D calculations for TE polarization, and a comparison of the  
415 calculated field components of the even and odd waveguide modes are presented. We also  
416 explain the spectroscopic polarimetry method in more detail.

417 This material is available free of charge via the Internet at <http://pubs.acs.org/>.

## 418 **Author Information**

### 419 **Corresponding Authors**

420 \*E-mail (A. Polman): polman@amolf.nl.

## 421 **Notes**

422 A.P. is co-founder and co-owner of Delmic BV, a startup company developing a commercial  
423 product based on the cathodoluminescence system that was used in this work.

## 424 **Acknowledgement**

425 We would like to acknowledge Toon Coenen, Mark W. Knight, Boris Le Feber and Sophie  
426 Meuret for useful discussions. This work is part of the research program of the “Stichting  
427 voor Fundamenteel Onderzoek der Materie (FOM)”, which is financially supported by the  
428 “Nederlandse Organisatie voor Wetenschappelijk Onderzoek (NWO)”. This work is part of  
429 NanoNextNL, a nanotechnology program funded by the Dutch ministry of economic affairs  
430 and is also supported by the European Research Council (ERC). DMB acknowledges support  
431 from a Marie-Curie Individual Fellowship QUIPS.

## 432 **References**

- 433 (1) Yablonovitch, E. Inhibited spontaneous emission in solid-state physics and electronics.  
434 *Phys. Rev. Lett.* **1987**, *58*, 2059.
- 435 (2) Yablonovitch, E. Photonic band-gap structures. *J. Opt. Soc. Am. B: Opt. Phys.* **1993**,  
436 *10*, 283–295.
- 437 (3) Blanco, A.; Chomski, E.; Grabtchak, S.; Ibisate, M.; John, S.; Leonard, S. W.;  
438 Lopez, C.; Meseguer, F.; Miguez, H.; Mondia, J. P.; Ozin, G. A.; Toader, O.; van  
439 Driel, H. M. Large-scale synthesis of a silicon photonic crystal with a complete three-  
440 dimensional bandgap near 1.5 micrometres. *Nature* **2000**, *405*, 437–440.
- 441 (4) Fujita, M.; Takahashi, S.; Tanaka, Y.; Asano, T.; Noda, S. Simultaneous inhibition and

- 442 redistribution of spontaneous light emission in photonic crystals. *Science* **2005**, *308*,  
443 1296–1298.
- 444 (5) Joannopoulos, J. D.; Johnson, S. G.; Winn, J. N.; Meade, R. D. *Photonic crystals:  
445 molding the flow of light*; Princeton University Press, 2011.
- 446 (6) Yoshie, T.; Scherer, A.; Hendrickson, J.; Khitrova, G.; Gibbs, H. M.; Rupper, G.;  
447 Ell, C.; Shchekin, O. B.; Deppe, D. G. Vacuum Rabi splitting with a single quantum  
448 dot in a photonic crystal nanocavity. *Nature* **2004**, *432*, 200–203.
- 449 (7) Akahane, Y.; Asano, T.; Song, B.-S.; Noda, S. High-Q photonic nanocavity in a two-  
450 dimensional photonic crystal. *Nature* **2003**, *425*, 944–947.
- 451 (8) Hughes, S. Enhanced single-photon emission from quantum dots in photonic crystal  
452 waveguides and nanocavities. *Opt. Lett.* **2004**, *29*, 2659–2661.
- 453 (9) Noda, S.; Yokoyama, M.; Imada, M.; Chutinan, A.; Mochizuki, M. Polarization mode  
454 control of two-dimensional photonic crystal laser by unit cell structure design. *Science*  
455 **2001**, *293*, 1123–1125.
- 456 (10) Park, H.-G.; Kim, S.-H.; Kwon, S.-H.; Ju, Y.-G.; Yang, J.-K.; Baek, J.-H.; Kim, S.-  
457 B.; Lee, Y.-H. Electrically driven single-cell photonic crystal laser. *Science* **2004**, *305*,  
458 1444–1447.
- 459 (11) Hirose, K.; Liang, Y.; Kurosaka, Y.; Watanabe, A.; Sugiyama, T.; Noda, S. Watt-  
460 class high-power, high-beam-quality photonic-crystal lasers. *Nat. Photonics* **2014**, *8*,  
461 406–411.
- 462 (12) Liles, A. A.; Debnath, K.; O’Faolain, L. Lithographic wavelength control of an external  
463 cavity laser with a silicon photonic crystal cavity-based resonant reflector. *Opt. Lett.*  
464 **2016**, *41*, 894–897.

- 465 (13) Krauss, T. F. Slow light in photonic crystal waveguides. *J. Phys. D: Appl. Phys.* **2007**,  
466 *40*, 2666.
- 467 (14) Krauss, T. F.; Richard, M.; Brand, S. Two-dimensional photonic-bandgap structures  
468 operating at near-infrared wavelengths. *Nature* **1996**, *383*, 699–702.
- 469 (15) Notomi, M.; Yamada, K.; Shinya, A.; Takahashi, J.; Takahashi, C.; Yokohama, I.  
470 Extremely large group-velocity dispersion of line-defect waveguides in photonic crystal  
471 slabs. *Phys. Rev. Lett.* **2001**, *87*, 253902.
- 472 (16) Vlasov, Y. A.; O’Boyle, M.; Hamann, H. F.; McNab, S. J. Active control of slow light  
473 on a chip with photonic crystal waveguides. *Nature* **2005**, *438*, 65–69.
- 474 (17) Mazoyer, S.; Baron, A.; Hugonin, J.-P.; Lalanne, P.; Melloni, A. Slow pulses in disor-  
475 dered photonic-crystal waveguides. *Appl. Opt.* **2011**, *50*, G113–G117.
- 476 (18) Beggs, D. M.; Rey, I. H.; Kampfrath, T.; Rotenberg, N.; Kuipers, L.; Krauss, T. F.  
477 Ultrafast tunable optical delay line based on indirect photonic transitions. *Phys. Rev.*  
478 *Lett.* **2012**, *108*, 213901.
- 479 (19) Gersen, H.; Karle, T.; Engelen, R.; Bogaerts, W.; Korterik, J.; Van Hulst, N.;  
480 Krauss, T.; Kuipers, L. Real-space observation of ultraslow light in photonic crystal  
481 waveguides. *Phys. Rev. Lett.* **2005**, *94*, 073903.
- 482 (20) Baba, T. Slow light in photonic crystals. *Nat. Photonics* **2008**, *2*, 465–473.
- 483 (21) Morichetti, F.; Ferrari, C.; Canciamilla, A.; Melloni, A. The first decade of coupled  
484 resonator optical waveguides: bringing slow light to applications. *Laser Photonics Rev.*  
485 **2012**, *6*, 74–96.
- 486 (22) Melloni, A.; Canciamilla, A.; Ferrari, C.; Morichetti, F.; O’Faolain, L.; Krauss, T.;  
487 De La Rue, R.; Samarelli, A.; Sorel, M. Tunable delay lines in silicon photonics: coupled  
488 resonators and photonic crystals, a comparison. *IEEE Photonics J.* **2010**, *2*, 181–194.

- 489 (23) Zabelin, V.; Dunbar, L. A.; Le Thomas, N.; Houdré, R.; Kotlyar, M. V.; O’Faolain, L.;  
490 Krauss, T. F. Self-collimating photonic crystal polarization beam splitter. *Opt. Lett.*  
491 **2007**, *32*, 530–532.
- 492 (24) Beggs, D. M.; White, T. P.; O’Faolain, L.; Krauss, T. F. Ultracompact and low-power  
493 optical switch based on silicon photonic crystals. *Opt. Lett.* **2008**, *33*, 147–149.
- 494 (25) Corcoran, B.; Monat, C.; Grillet, C.; Moss, D. J.; Eggleton, B. J.; White, T.;  
495 O’Faolain, L.; Krauss, T. F. Green light emission in silicon through slow-light enhanced  
496 third-harmonic generation in photonic-crystal waveguides. *Nat. Photonics* **2009**, *3*,  
497 206–210.
- 498 (26) Pohl, D. W.; Denk, W.; Lanz, M. Optical stethoscopy: Image recording with resolution  
499  $\lambda/20$ . *Appl. Phys. Lett.* **1984**, *44*, 651–653.
- 500 (27) Betzig, E.; Trautman, J. K.; Harris, T. D.; Weiner, J. S.; Kostelak, R. L. Breaking  
501 the diffraction barrier: optical microscopy on a nanometric scale. *Science* **1991**, *251*,  
502 1468–1470.
- 503 (28) Reddick, R. C.; Warmack, R. J.; Ferrell, T. L. New form of scanning optical microscopy.  
504 *Phys. Rev. B* **1989**, *39*, 767.
- 505 (29) Chicanne, C.; David, T.; Quidant, R.; Weeber, J.-C.; Lacroute, Y.; Bourillot, E.;  
506 Dereux, A.; Colas des Francs, G.; Girard, C. Imaging the local density of states of  
507 optical corrals. *Phys. Rev. Lett.* **2002**, *88*, 097402.
- 508 (30) Colas des Francs, G.; Girard, C.; Weeber, J.-C.; Dereux, A. Relationship between  
509 scanning near-field optical images and local density of photonic states. *Chem. Phys.*  
510 *Lett.* **2001**, *345*, 512–516.
- 511 (31) Novotny, L. The history of near-field optics. *Prog. Optics* **2007**, *50*, 137.

- 512 (32) Le Feber, B.; Rotenberg, N.; Beggs, D. M.; Kuipers, L. Simultaneous measurement of  
513 nanoscale electric and magnetic optical fields. *Nat. Photonics* **2014**, *8*, 43–46.
- 514 (33) García de Abajo, F. J. Optical excitations in electron microscopy. *Rev. Mod. Phys.*  
515 **2010**, *82*, 209–275.
- 516 (34) Sapienza, R.; Coenen, T.; Renger, J.; Kuttge, M.; van Hulst, N. F.; Polman, A. Deep-  
517 subwavelength imaging of the modal dispersion of light. *Nat. Mater.* **2012**, *11*, 781–787.
- 518 (35) Brenny, B. J. M.; Polman, A.; García de Abajo, F. J. Femtosecond plasmon and photon  
519 wave packets excited by a high-energy electron on a metal or dielectric surface. *submitted*  
520 **2016**,
- 521 (36) Losquin, A.; Kociak, M. Link between cathodoluminescence and electron energy loss  
522 spectroscopy and the radiative and full electromagnetic local density of states. *ACS*  
523 *Photonics* **2015**, *2*, 1619–1627.
- 524 (37) Osorio, C. I.; Coenen, T.; Brenny, B. J. M.; Polman, A.; Koenderink, A. F. Angle-  
525 resolved cathodoluminescence imaging polarimetry. *ACS Photonics* **2016**, *3*, 147–154.
- 526 (38) Spirkoska, D. et al. Structural and optical properties of high quality zinc-  
527 blende/wurtzite GaAs nanowire heterostructures. *Phys. Rev. B* **2009**, *80*, 245325.
- 528 (39) Zhu, X. L.; Ma, J. S., Y. Zhang; Xu, X. F., J. Wu; Zhang, Y.; Han, X. B.; Fu, Q.;  
529 Liao, Z. M.; Chen, L.; Yu, D. P. Confined three-dimensional plasmon modes inside a  
530 ring-shaped nanocavity on a silver film imaged by cathodoluminescence microscopy.  
531 *Phys. Rev. Lett.* **2010**, *105*, 127402.
- 532 (40) Bashevoy, M. V.; Jonsson, F.; MacDonald, K. F.; Chen, Y.; Zheludev, N. I. Hyper-  
533 spectral imaging of plasmonic nanostructures with nanoscale resolution. *Opt. Express*  
534 **2007**, *15*, 11313–11320.

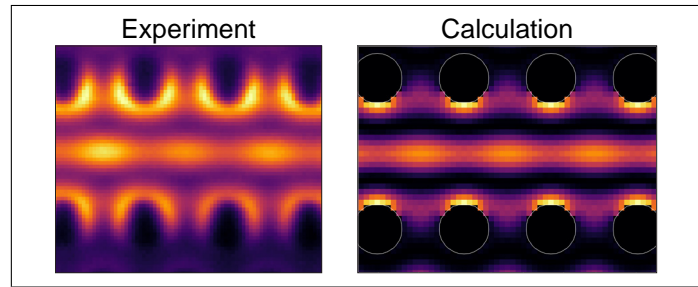
- 535 (41) Adamo, G.; Ou, J. Y.; So, J. S.; Jenkins, S. D.; De Angelis, F.; MacDonald, K. F.;  
536 Di Fabrizio, E.; Ruostekoski, J.; Zheludev, N. I. Electron-beam-driven collective-mode  
537 metamaterial light source. *Phys. Rev. Lett.* **2012**, *109*, 217401.
- 538 (42) Yamamoto, N.; Ohtani, S.; García de Abajo, F. J. Gap and Mie plasmons in individual  
539 silver nanospheres near a silver surface. *Nano Lett.* **2011**, *11*, 91–95.
- 540 (43) Myroshnychenko, V.; Nelayah, J.; Adamo, G.; Geuquet, N.; Rodríguez-Fernández, J.;  
541 Pastoriza-Santos, I.; MacDonald, K. F.; Henrard, L.; Liz-Marzán, L. M.; Zheludev, N. I.;  
542 Kociak, M.; García de Abajo, F. J. Plasmon spectroscopy and imaging of individual gold  
543 nanodecahedra: a combined optical microscopy, cathodoluminescence, and electron  
544 energy-loss spectroscopy study. *Nano Lett.* **2012**, *12*, 4172–4180.
- 545 (44) Knight, M. W.; Liu, L.; Wang, Y.; Brown, L.; Mukherjee, S.; King, N. S.; Everitt, H. O.;  
546 Nordlander, P.; Halas, N. J. Aluminum plasmonic nanoantennas. *Nano Lett.* **2012**, *12*,  
547 6000–6004.
- 548 (45) Takeuchi, K.; Yamamoto, N. Visualization of surface plasmon polariton waves in two-  
549 dimensional plasmonic crystal by cathodoluminescence. *Opt. Express* **2011**, *19*, 12365–  
550 12374.
- 551 (46) Honda, M.; Yamamoto, N. Size dependence of surface plasmon modes in one-  
552 dimensional plasmonic crystal cavities. *Opt. Express* **2013**, *21*, 11973–11983.
- 553 (47) Ma, X.; Grüßer, M.; Schuster, R. Angular Dependence of Cathodoluminescence of Lin-  
554 ear and Circular Au Gratings: Imaging the Coupling Angles between Surface Plasmon  
555 Polaritons and Light. *J. Phys. Chem. C* **2014**, *118*, 23247–23255.
- 556 (48) Benisty, H. Modal analysis of optical guides with two-dimensional photonic band-gap  
557 boundaries. *J. Appl. Phys.* **1996**, *79*, 7483–7492.

- 558 (49) Johnson, S. G.; Villeneuve, P. R.; Fan, S.; Joannopoulos, J. D. Linear waveguides in  
559 photonic-crystal slabs. *Phys. Rev. B* **2000**, *62*, 8212.
- 560 (50) Lecamp, G.; Hugonin, J.-P.; Lalanne, P. Theoretical and computational concepts for  
561 periodic optical waveguides. *Opt. Express* **2007**, *15*, 11042–11060.
- 562 (51) Johnson, S. G.; Joannopoulos, J. D. Block-iterative frequency-domain methods for  
563 Maxwell’s equations in a planewave basis. *Opt. Express* **2001**, *8*, 173–190.
- 564 (52) Beggs, D. M.; O’Faolain, L.; Krauss, T. F. Accurate determination of the functional  
565 hole size in photonic crystal slabs using optical methods. *Phot. Nano. Fund. Appl.*  
566 **2008**, *6*, 213–218.
- 567 (53) Lončar, M.; Nedeljković, D.; Pearsall, T. P.; Vučković, J.; Scherer, A.; Kuchinsky, S.;  
568 Allan, D. C. Experimental and theoretical confirmation of Bloch-mode light propagation  
569 in planar photonic crystal waveguides. *Appl. Phys. Lett.* **2002**, *80*, 1689–1691.
- 570 (54) Coenen, T.; Vesseur, E. J. R.; Polman, A. Angle-resolved cathodoluminescence spec-  
571 troscopy. *Appl. Phys. Lett.* **2011**, *99*, 143103.
- 572 (55) Vesseur, E. J. R.; Polman, A. Plasmonic whispering gallery cavities as optical antennas.  
573 *Nano Lett.* **2011**, *11*, 5524–5530.
- 574 (56) Coenen, T.; Polman, A. Polarization-sensitive cathodoluminescence Fourier microscopy.  
575 *Opt. Express* **2012**, *20*, 18679–19691.
- 576 (57) Born, M.; Wolf, E. *Principles of Optics: Electromagnetic Theory of Propagation, In-*  
577 *terference and Diffraction of Light*, 7<sup>th</sup> ed.; Cambridge University Press, 1997.
- 578 (58) Brenny, B. J. M.; Coenen, T.; Polman, A. Quantifying coherent and incoherent cathodo-  
579 luminescence in semiconductors and metals. *J. Appl. Phys.* **2014**, *115*, 244307.

- 580 (59) Paniagua-Domínguez, R.; Grzela, G.; Gómez Rivas, J.; Sánchez-Gil, J. Enhanced and  
581 directional emission of semiconductor nanowires tailored through leaky/guided modes.  
582 *Nanoscale* **2013**, *5*, 10582–10590.
- 583 (60) Abujetas, D. R.; Paniagua-Domínguez, R.; Sánchez-Gil, J. A. Unraveling the janus role  
584 of Mie resonances and leaky/guided modes in semiconductor nanowire absorption for  
585 enhanced light harvesting. *ACS Photonics* **2015**, *2*, 921–929.
- 586 (61) Le Thomas, N.; Houdré, R.; Frandsen, L. H.; Fage-Pedersen, J.; Lavrinenko, A. V.;  
587 Borel, P. I. Grating-assisted superresolution of slow waves in Fourier space. *Phys. Rev.*  
588 *B* **2007**, *76*, 035103.
- 589 (62) Jágorská, J.; Le Thomas, N.; Houdré, R.; Beggs, D. M.; O'Brien, D.; Krauss, T. F.  
590 Coupling length of silicon-on-insulator directional couplers probed by Fourier-space  
591 imaging. *Appl. Phys. Lett.* **2008**, *92*, 151106.

592 **Graphical TOC Entry**

593



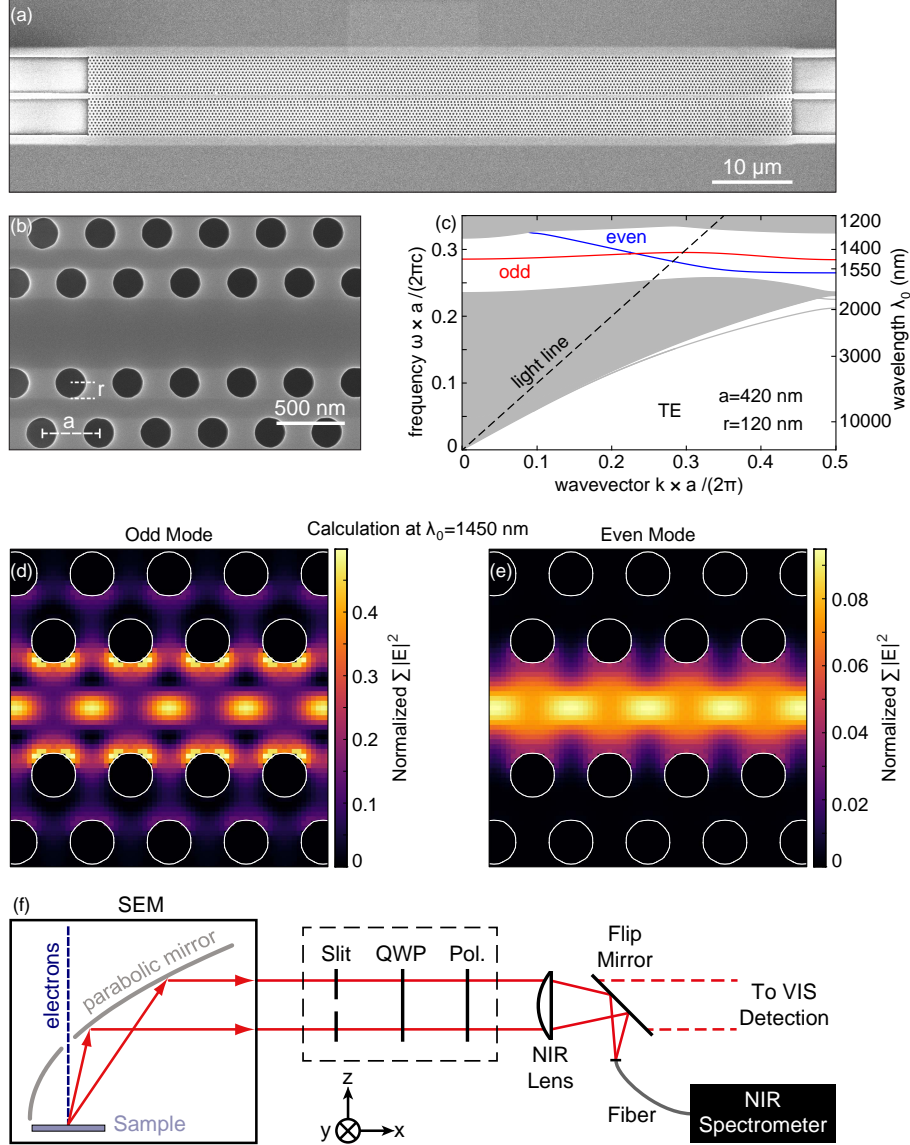


Figure 1: (a) Scanning electron micrograph of one of the silicon PCWGs on sample 1 studied here. A 90  $\mu\text{m}$  long, 10  $\mu\text{m}$  wide, and 220 nm thick waveguide with a hexagonal lattice of holes is suspended above a substrate of silica on silicon. (b) Close-up micrograph of waveguide WG2, with a period of  $a=420$  nm and a hole radius of  $r=120$  nm. (c) Band diagram of the waveguide from (b), for TE polarization. The gray regions denote the continuum of available modes above and below the photonic band gap, within which we distinguish an even (blue) and odd (red) waveguide mode. The black dashed line corresponds to the light line of air. (d,e) Calculation of the modal intensity distributions of the odd (e) and even (f) waveguide modes, for  $\lambda_0=1450$  nm, normalized to the maximum intensity for all polarizations and wavelengths. The white circles show the positions of the holes. (f) Schematic of the cathodoluminescence spectroscopy system. The 30 keV electron beam excites the sample, a parabolic mirror collects the emitted radiation and directs it to an optical setup. Here we can focus the light onto a NIR spectrometer or filter the emitted beam with a (vertically oriented) slit and measure the full polarization state using a quarter-wave plate and linear polarizer. The PCWGs for all measurements in the main text are oriented along the y-axis of the coordinate system.

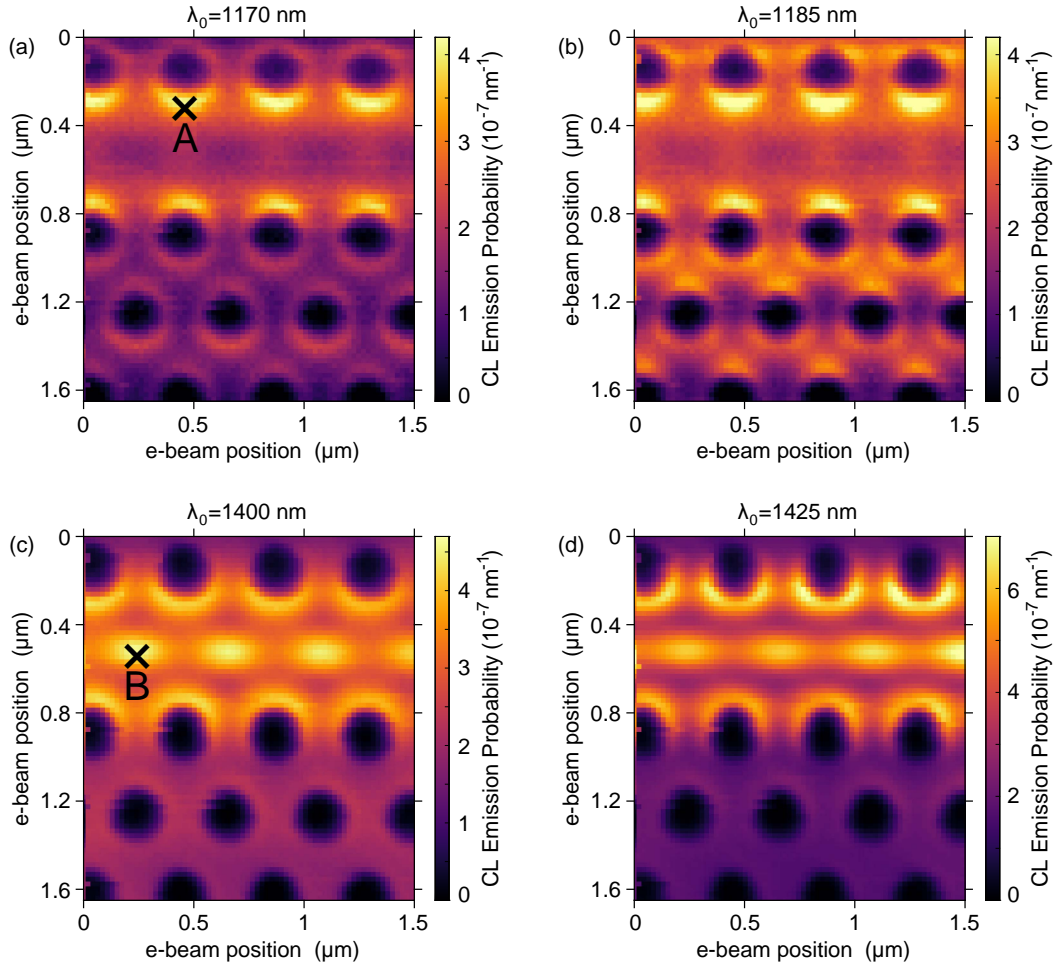


Figure 2: Measured CL emission probability of WG2, as a function of wavelength and excitation position, for center wavelengths of  $\lambda_0=1170$  nm (a),  $\lambda_0=1185$  nm (b),  $\lambda_0=1400$  nm (c), and  $\lambda_0=1425$  nm (d) (20 nm bandwidth). Black crosses denote the two locations for which we show spectra in Figure 3.

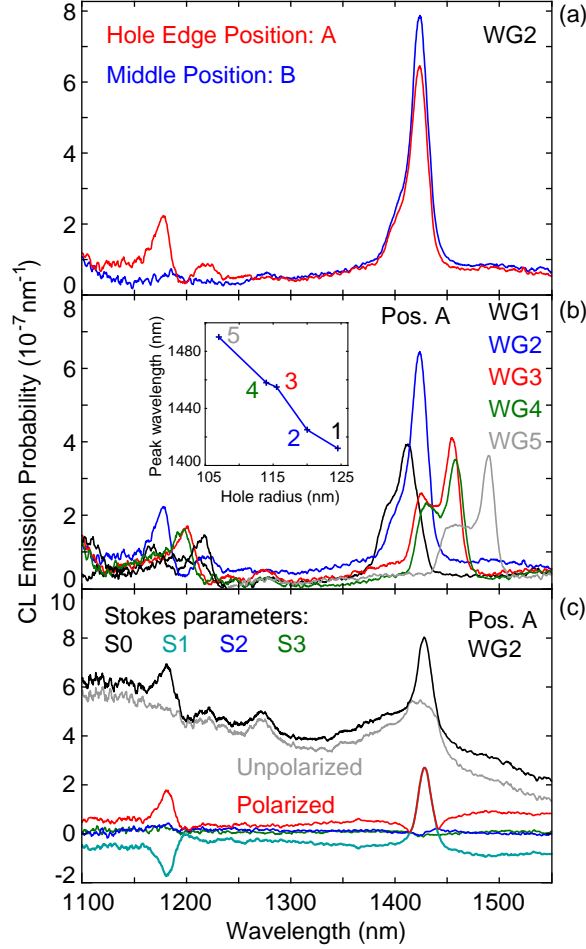


Figure 3: (a) CL emission probability as a function of wavelength, measured on WG2, comparing the spectra obtained for two different excitations positions A (red) and B (blue) indicated in Figure 2. (b) CL spectra obtained for excitation position A on five different waveguides (WG1–WG5) with different hole size. The inset shows the wavelength of the dominant peak as a function of hole radius. (c) Polarization-filtered spectra measured on WG2 for excitation position A. We determine the Stokes parameters S0 (black), S1 (turquoise), S2 (blue) and S3 (green) and use them to separate the polarized contribution (red) from the unpolarized contribution that is due to the background luminescence from the substrate (gray). We note that S1 and the polarized contribution overlap at  $\lambda_0 \sim 1425$  nm.

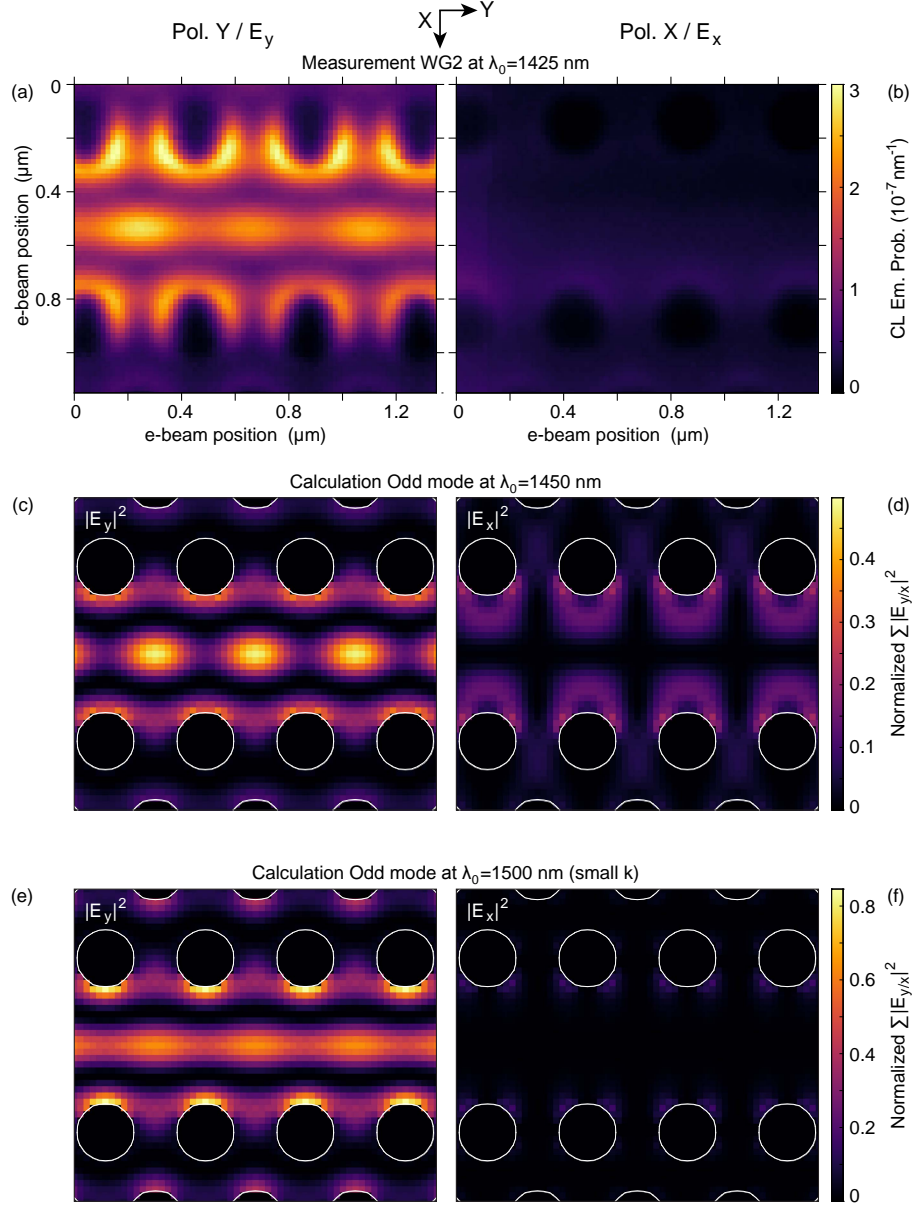


Figure 4: Polarization-filtered 2D excitation maps of WG2, showing the CL emission probability as a function of the electron beam position for a center wavelength of  $\lambda_0=1425$  nm, averaged over a 20 nm bandwidth. Only a linear polarizer was used here. The polarization is horizontal along the waveguide (along y) for (a) and vertical (along x) for (b) and the two are shown on the same intensity scale. (c) Calculation of the field intensity  $|E_y|^2$  for the odd waveguide mode at  $\lambda_0=1450$  nm and the corresponding calculation for  $|E_x|^2$  (d), integrated over  $k$  within the frequency range, both shown on the same scale normalized to the overall total maximum intensity for all the calculations. We show  $|E_y|^2$  (e) and  $|E_x|^2$  (f) on the same scale for the odd mode calculated at  $\lambda_0=1500$  nm, integrated (within the frequency range) over a range of  $k$  close to 0, above the light line. The distributions for  $k$  below the light line can be seen in Figure S7 of the Supporting Information.